Journal of Physics B: Atomic, Molecular and Optical Physics

Looking inside the tunnelling barrier: II. Co- and counter-rotating electrons at the 'tunnelling exit'

To cite this article: Jivesh Kaushal and Olga Smirnova 2018 *J. Phys. B: At. Mol. Opt. Phys.* **51** 174002

OPEN ACCESS
IOP Publishing
Journal of Physics B: Atomic, Molecular and Optical Physics
J. Phys. B: At. Mol. Opt. Phys. **51** (2018) 174002 (15pp)
https://doi.org/10.1088/1361-6455/aad132

Looking inside the tunnelling barrier: II. Co- and counter-rotating electrons at the 'tunnelling exit'

Jivesh Kaushal[1,3] **and Olga Smirnova**[1,2]

[1] Max-Born-Institut, Max-Born-Str. 2A, D-12489 Berlin, Germany
[2] Technische Universität Berlin, Ernst-Ruska-Gebaüde, Hardenbergstr. 36A, D-10623 Berlin, Germany

E-mail: jivesh.kaushal@mbi-berlin.de and olga.smirnova@mbi-berlin.de

Received 12 February 2018, revised 7 June 2018
Accepted for publication 4 July 2018
Published 3 August 2018

Abstract

The initial conditions for electron trajectories at the exit from the tunnelling barrier are often used in strong field models, for example to bridge the first and the second steps of the three-step model celebrated in this issue. Since the analytical *R*-matrix theory does not rely on the three-step model or the concept of the tunnelling barrier in coordinate space, obtaining the initial conditions for electron trajectories at the barrier exit is, strictly speaking, not necessary to calculate standard observables. Not necessary, but possible—especially when motivated by the occasion of this issue. The opportunity to evaluate such initial conditions emerges as a corollary of analysing sub-barrier kinematics, which includes the interplay of laser and Coulomb fields on the sub-cycle scale (see the companion paper I). We apply our results to discuss the difference in such initial conditions for co- and counter-rotating electrons liberated during strong field ionisation. We derive quantum orbits and classical trajectories describing ionization dynamics of co- and counter-rotating electrons in long-range potentials.

Keywords: strong field ionisation, optical tunnelling, non-adiabatic Coulomb effects

(Some figures may appear in colour only in the online journal)

1. Introduction

The trajectory-based picture of strong field phenomena has been very inspiring and useful. It underlies our intuitive understanding of all strong field phenomena: single, double and multiple ionisation [1–5], high harmonic generation [6–10], above threshold ionisation [11–16] and related attosecond imaging techniques, such as laser-induced diffraction [17–20], holography [17, 21, 22], attoclock [23, 24], high harmonic spectroscopy [18, 25–36, 37–43], to name but a few examples. Strong field ionisation is the first step in all these phenomena.

Since the pioneering work of Keldysh [44] and PPT [45–47], the physical picture of strong field ionisation has inevitably involved complex times (see recent reveiw [48]). The complex times are associated with optical tunnelling. The barrier created by the oscillating low-frequency field and the core potential separates classically forbidden and allowed regions. The separation point in space is called 'the exit from the barrier'.

This image is compelling in low-frequency fields $\omega \ll I_p$, where optical tunnelling is the dominant ionisation mechanism. One reason why tunnelling emerges as the dominant mechanism is that real excitations within the potential well are strongly suppressed in the low-frequency regime. In fact, both tunnelling and multiphoton regimes of strong field ionisation in the Keldysh theory involve electron dynamics in the sub-barrier region (see [49]).

Tunnelling and associated complex times lead to complex trajectories, even in the simplest case of a short-range potential. Looking broadly, the interplay of classically

[3] Author to whom any correspondence should be addressed.

allowed and classically forbidden regions of particle dynamics always leads to complex trajectories in the semiclassical limit (see e.g. Keller in [50, p 27]), see also [51, 52]). However, in those problems the 'barrier', i.e. the separation between the forbidden and the allowed regions, is time-independent. For example, in scattering theory, the semiclassical description of the Rutherford scattering [52] leads to complex trajectories due to the presence of classically inaccessible regions in the momentum space ('dynamical tunnelling'). In geometrical optics, where rays are used to assemble electromagnetic fields, representing the main term in the semiclassical expansion of the exact fields, the complex rays accurately describe electromagnetic fields on the dark side of caustics and refraction shadows, i.e. in classically forbidden regions [50, 51]. Here the role of time is played by the distance along the ray and it becomes complex once a classically forbidden region is involved. Formally, complex-valued variables originate from the fact that those kinds of trajectories are derived from action, which becomes imaginary in the classically forbidden region. The imaginary action describes exponential damping of a signal inside the classically forbidden region. For example, real-values rays are tangent to the caustic on its convex part (bright side of the caustic), while only complex-valued rays can be tangent to the caustic on its concave part (the dark side of the caustic).

In the case of strong field ionisation, complex trajectories, especially complex-valued coordinates, appear as a manifestation of the non-adiabaticity of the electron dynamics triggered by rapid changes of the tunnelling barrier due to fast oscillations of the laser field or quickly the changing field envelope, in the case of nearly single-cycle pulses. Of course, this does not make strong field complex trajectories any less 'legal' than the real-valued ones. The "complexity" of the coordinate becomes particularly acute when the coordinate-dependent Coulomb potential is included into analysis.

From the pragmatic perspective of a semiclassical theory, such as e.g. the analytical *R*-matrix (A*R*M) theory, complex electron trajectories take care of the propagation of the electron wave function in time in the same way as complex rays take care of the propagation of the electromagnetic fields in space (Keller in [50, 51]). From the practical perspective and following the tradition in the field, it is desirable to introduce effective classical, i.e. real-valued trajectories, which start at the time of the exit from the barrier with some initial conditions encoding the information about the under-the-barrier quantum dynamics, propagate in the laser and the Coulomb fields (or in a more complex field decribing the electron-core interaction) according to Newton's equations, and are uniquely linked to a given observable (e.g. the photoelectron momentum) at the detector. Establishing trajectories linked to final photoelectron momenta helps one to understand the ionization dynamics. Last but not least, such trajectories should include information about the intial orbital, e.g. the orbital momentum and its projection on the quantization axis.

This desire is a very natural one, and the question 'what is the value of the electron velocity for *such trajectory* at the 'exit' from the tunnelling barrier for a given final momentum [53–57]?' is hardly new. If the Coulomb potential is not included, the formal answer can be obtained with no effort and it is known since the PPT times [45–47, 58]: for the peak of the photoelectron distribution the 'exit velocity' is equal to zero. (It only means that the trajectory with zero intial velocity accurately follows the peak of the quantum phase-space distribution sufficiently far from the exit coordinate, see e.g. Ref. [59], Figure 6, and Ref. [60]). Once the Coulomb potential is taken into account, the analysis becomes more involved.

In strong fields we usually speak about Coulomb 'corrections', because the electron dynamics is dominated by the laser field. However, these 'corrections' become very significant in the sub-barrier region, where the electron comes very close to the singular Coulomb core. The problem can be solved, for example, using the ideas of the *ab initio R*-matrix method [61], where the configuration space around the core and outside the core is treated by applying different approximations. We apply the same trick in the A*R*M method [62–68], see also recent work [69] similar to [68] . Then, we have to match the solutions for the electron wave functions at the boundary of the inner and outer regions.

The A*R*M method starts with the time-dependent Schrödinger equation, but ends up with semiclassical expressions. Celebrating 25 years of the three-step model, we shall keep things simple in this paper, making the short-cut directly to the semiclassical picture. The semiclassical ansatz represents the electron wave function in terms of a phase (action) and an amplitude (prefactor, which is linked to the electron density). It means that we have to match both the phase and the amplitude (the gradient of the phase) at the *R*-matrix boundary which separates the inner and the outer regions. The key idea for matching the phase has already been given in the PPT papers [45–47, 58]. We just had to adapt it to our formalism and extend to the sub-cycle regime [62, 64]. Matching the gradient of the phase proved to be a harder task, because the gradient of the Coulomb potential—the attractive force responsible for the momentum shift—becomes very strong as we approach the core. Nevertheless, the problem was solved in [67].

In fact, the outcome of the matching procedure can be understood as specification of the time, velocity and coordinate at the effective 'entrance' to the barrier (the effective start of the electron trajectory leaving the core). For the short-range potential, this 'entrance' lies at the origin, but it is shifted from the origin in case of the the Coulomb potential. Knowing the starting position, velocity, and time allows one to find the corresponding parameters at the 'exit' from the barrier, the latter defined at the instant when the imaginary part of the time along the trajectory turns to zero.

These 'initial values' at the 'barrier entrance' do not contribute to observables in the case of ionisation from the *s*-states, which has been analysed within the A*R*M method in [65, 66, 70]. However, they are still needed if one wants to establish the 'initial conditions' at the exit from the barrier, even for *s*-states.

The situation changes with ionisation from states with non-zero *l*, *m*. Now the the initial velocity 'at the entrance' and the 'entrance time' directly contribute to the ionisation

rates for orbitals with $m \neq 0$ in circularly polarised fields. The contributions depend on the l, m quantum numbers of the initial orbital and leave their mark in photoelectron spectra. Since these quantities contribute to observables, they have to be calculated.

In our first paper [64] on A*R*M theory for ionisation in circularly polarised fields, we resorted to estimates for the 'most popular' trajectory, which is followed by the majority of the electrons and which has no non-adiabatic features (this trajectory 'yields' the peak in the photoelectron spectrum in circularly polarised fields). Later, we rigorously performed the required matching in [67]. The resulting momentum shifts, accumulated under the barrier, are intrinsically sub-cycle and sensitive to orbital geometry.

Due to the fact that we have explicitly derived the velocity, time and coordinate 'at the entrance to the barrier' in A*R*M formalism, we can define a unique quantum trajectory, which satisfies the Newtons equations with the Coulomb and the laser fields included, starts at the 'entrance to the barrier' and terminates at the detector with a given final momentum. The trajectory is quantum, because it evolves in complex time and space. Moreover, the evolution of the imaginary and real parts of the trajectory coordinate are now coupled via the long-range potential. This coupling persists until the end of the laser pulse, affects the population amplitudes associated with the trajectories, and reflects the fact that ionisation is not completed at the 'exit from the barrier'. For example, electrons can be trapped into Rydberg states and released later at times $t > t_{exit}$ [65]. In other words, there is no such moment in time after which the electron dynamics is fully described by a purely classical trajectory.

However, if one insists on establishing a fully classical trajectory propagating in real time and space after the 'exit', encoding the information about the sub-barrier dynamics only in the exit velocities and exit coordinates, it is also possible. Such trajectory, while imperfect, is also uniquely defined. The imperfection is due to the missing imaginary part of the coordinate associated with the quantum trajectory and the missing coupling between its real and imaginary parts. At the time of exit from the barrier, the coordinate of the classical trajectory is set to be equal to the real part of the coordinate of the quantum trajectory. However, the velocity of classical trajectory at the exit time is not identical to the velocity of quantum trajectory at the same time—they must only coincide at the detector.

We stress again that, strictly speaking, neither the quantum nor the classical trajectory are needed to obtain observables in the A*R*M theory. Their purpose is different. First, they are introduced here to explore how far can we push the language of trajectories including the Coulomb and the laser field for quantitatively describing the ionisation dynamics in strong laser fields. Second, they provide insight into ionisation dynamics from current-carrying orbitals, allowing us to interpret ionisation of co- and counter-rotating electrons from the trajectory perspective.

We use atomic units ($m_e = \hbar = k_e = 1$), and consider here only circularly polarised fields.

2. A*R*M perspective on electron velocities and coordinates at the exit from the barrier

2.1. Sub-cycle Coulomb corrections to ionisation times

In the A*R*M theory we include the effects of Coulomb potential $U(r) = -Z/r$ in the outer region up to the first order in Z, in the wave function's exponent (action). In the inner region, the Coulomb effects are included fully. It leads to the shift of the saddle points in the time-domain quantum integrals over the ionisation times. In particular the complex ionisation time becomes $t^* \equiv t_s^c \equiv t_s + \Delta t_s^c$ [64, 66, 67, 70]. Since the PPT times, this time is associated with the beginning of tunnelling. Here t_s is the SFA ionisation time for a short-range potential, while Δt_s^c is the Coulomb correction to this time. For the same final electron momentum at the detector, the trajectory starts earlier w.r.t to the SFA (short-range) case. The correction Δt_s^c is given by equation (13) in appendix A of [71], which we rewrite here:

$$\Delta t_s^c = -\frac{\mathbf{v}_\mathbf{k}(t_s) \cdot \Delta \mathbf{v}^c}{\mathbf{v}_\mathbf{k}(t_s) \cdot \mathbf{E}_L(t_s)}, \tag{1}$$

or, in the equivalent form [66, 67, 70]:

$$\Delta t_s^c = -\frac{dW_C(\mathbf{k}, t_s)}{dI_p}\bigg|_{\kappa=\text{const}}, \tag{2}$$

where $\kappa = \sqrt{2I_p}$ and the phase $W_C(\mathbf{k}, t_s)$ is the Coulomb correction to the SFA action in the A*R*M theory:

$$W_C(\mathbf{k}, t_s^c) = -\int_{t_\kappa}^{t} dt\; U(\mathbf{r}_L^s(t)),\; t_\kappa = t_s - i\kappa^{-2}. \tag{3}$$

This term describes the Coulomb-laser coupling, and amounts to integrating the Coulomb potential along the trajectory $\mathbf{r}_L^s(t)$ of free electron in the laser field:

$$\mathbf{r}_L^s(t) = \int_{t_s}^{t} \mathbf{k} + \mathbf{A}(\xi) d\xi. \tag{4}$$

Because the Coulomb-laser coupling term originates from the outer region, any further correction to the trajectory would involve second and higher order terms in Z, which are much smaller for direct electrons and field frequency $\omega \ll I_p \equiv \kappa^2/2$, where I_p is the ionisation potential.

2.2. Sub-cycle Coulomb corrections to the initial velocity

The initial velocity at complex ionisation time t_s^c enters the expression for the ionisation amplitudes [67] and rates (equations (4) and (5) in [71]) via the term $e^{im\phi_v^c(t_s^c)}$, where $\phi_v^c(t_s^c)$ is the complex tunnelling angle, $\tan\phi_v^c(t_s^c) = \frac{v_\parallel(t_s^c)}{v_\perp(t_s^c)}$— the angle at which the electron enters the classically forbidden region. Here $v_\parallel(t_s^c)$ and $v_\perp(t_s^c)$ are the initial velocities parallel and perpendicular to field direction at time t_s^c. The perpendicular velocity is positive if it has positive projection on the final momentum. Finally, m is the magnetic quantum number of the ionising bound state. For orbitals with $m = 0$, this Coulomb correction to momentum has no impact on final observables at the detector, i.e. the photoelectron spectrum.

For $\ell \neq 0$ and $m \neq 0$ bound states, the Coulomb-laser coupling leads to a momentum shift, $\Delta\mathbf{v}^c(T)$ [67]:

$$\Delta\mathbf{v}^c(t_Q, T) = -\int_{t_Q}^{T} dt\ \nabla U(\mathbf{r}_L^s(t)) - \mathbf{v}_\mathbf{k}(t_s),\ t_Q = t_s - i\frac{Q}{\kappa^3}, \quad (5)$$

$\mathbf{v}_\mathbf{k}^2(t_s) = -2I_p$ which modifies the initial velocity at time t_s^c:

$$\mathbf{v}(t_s^c) = \mathbf{k} + \mathbf{A}(t_s^c) - \Delta\mathbf{v}^c(t_Q, T). \quad (6)$$

Time t_Q is an outcome of the matching procedure. Here Q is the effective charge of the core which describes the behaviour of the bound wave function in the classically forbidden region, $I_p = Q/2\nu^2$, where $\nu = \sqrt{Q/2I_p}$ is the effective quantum number. For short-range potential $Q = 0$, $\nu = 0$. Note that $\lim_{Q\to 0}\Delta\mathbf{v}^c(t_Q, T) \to 0$ (see appendix 2, [67]). The physical meaning of this expression is as follows: the electron momentum $\mathbf{k}$ is fixed at the detector. The first term $\mathbf{k} + \mathbf{A}(t_s^c)$ describes the SFA velocity at the Coulomb-corrected complex ionisation time t_s^c. The term $\Delta\mathbf{v}^c(t_Q, T)$ describes the momentum shift accumulated due to the Coulomb-laser coupling on the way from the origin to detector. Because the final momentum is fixed to be $\mathbf{k}$, the initial velocity subtracts $\Delta\mathbf{v}^c(t_Q, T)$ to compensate this 'future' change in velocity.

The above expressions are valid for arbitrary field geometries (for direct electrons), all electron momenta, and for all values of the Keldysh parameter γ within the applicability of the theory. The latter requires that real transitions to excited states are negligible. In practice, this of course limits the region of available frequencies and laser intensities (usually $\omega \ll \kappa^2/2$).

2.3. Properties of classical and quantum trajectories

In the previous two subsections we defined the complex ionisation time and the electron velocity at this time. Both quantities directly enter the A*R*M expression for ionisation amplitudes and contribute to the photoelectron spectra.

Now we aim to introduce auxiliary tool—quantum and classical trajectories. They will allow us to interpret observables in terms of the Newtonian mechanics. Both quantum (complex) and classical (real) trajectories are evaluated in the first order with respect to Coulomb potential, to be consistent with the A*R*M approach.

The quantum trajectory starts at real coordinate $r_Q = Q/\kappa^2$ (along the axis defined by the laser field at time $\Re[t_s^C]$, but in the opposite direction) at the time $t_Q^c = t_Q + \Delta t_s^c$ with the velocity:

$$\mathbf{v}(t_Q^c) = \mathbf{v}_\mathbf{k}(t_Q^c) - \Delta\mathbf{v}^c(t_Q, T). \quad (7)$$

The velocity at any time $t > t_Q$ is:

$$\mathbf{v}(t) = \mathbf{v}_\mathbf{k}(t) - \Delta\mathbf{v}^c(t_Q, T) - \int_{t_Q}^{t} dt\ \nabla U(\mathbf{r}_L^s(t)) - \mathbf{v}_\mathbf{k}(t_s) \equiv \mathbf{v}^{FW}(t). \quad (8)$$

The coordinate r_Q, time t_Q and the respective initial velocity at this time are known due to the matching procedure. These quantities fully specify the quantum trajectory:

$$\mathbf{r}^Q(t) = \mathbf{r}_Q + \int_{t_Q^c}^{t} \mathbf{v}_\mathbf{k}(\tau)d\tau + \int_{t_Q}^{t} \mathbf{v}^c(\tau)d\tau, \quad (9)$$

where the Coulomb velocity is $\mathbf{v}^c(\tau) \equiv -\Delta\mathbf{v}^c(t_Q, T) - \int_{t_Q}^{t} dt\ \nabla U(\mathbf{r}_L^s(t)) - \mathbf{v}_\mathbf{k}(t_s)$.

Importantly, the A*R*M -trajectory $\mathbf{r}_L^s(t)$ which enters the argument of the Coulomb force $-\nabla U(\mathbf{r}_L^s(t))$ in the integral (equation (8)) is always complex, as discussed in the introduction. It remains complex, with constant imaginary part, even after the exit from the barrier during the real time evolution. It has implications for our ability to introduce an equivalent classical trajectory.

Indeed, taking into account the explicit expression for the velocity $\mathbf{v}(t)$ (equation (5)), we can rewrite (equation (8)) in the equivalent form:

$$\mathbf{v}(t) = \mathbf{v}_\mathbf{k}(t) + \int_{t}^{T} dt\ \nabla U(\mathbf{r}_L^s(t)) \equiv \mathbf{v}^{BW}(t). \quad (10)$$

The last equation simply describes back propagation of the final momentum $\mathbf{k}$ from time T at the end of the pulse to arbitrary time t. The velocities in equations (equations (8) and (10)) propagated forward from time t_Q and backward from time T will coincide at any point t if and only if the back propagation is performed along the complex trajectory $\mathbf{r}_L^s(t)$. This is the case for the quantum trajectory.

If we neglect the imaginary part of the trajectory $\mathbf{r}_L^s(t)$ during back propagation from the detector, as we have to do if we want to introduce a purely classical trajectory, we will have a velocity off-set between the inevitably quantum forward propagation (i.e. using complex A*R*M trajectories) from the 'under the barrier' region and the desirably classical backward propagation (i.e. using only real parts of A*R*M trajectories) back from the detector.

Nevertheless, the classical trajectory is also uniquely defined. Its initial coordinate is defined by the real part of the coordinate on quantum trajectory at the exit time: $\Re[\mathbf{r}^Q(t_{exit})]$. But the exit velocity is defined by $\mathbf{v}^{BW}(t_{exit})$ propagated backwards from the end of the laser pulse along the real trajectory. Such back propagation is necessary to make sure that the classical trajectory propagated from the 'barrier exit' to the detector will have correct final momentum $\mathbf{k}$ at time T. thus, the classical trajectory is uniquely derived from the quantum trajectory as follows:

$$\mathbf{r}^C(t) = \Re[\mathbf{r}^Q(\Re[t_s^c])] + \int_{\Re[t_s^c]}^{t} \mathbf{v}^C(\tau)d\tau, \quad (11)$$

where $t_{exit} \equiv \Re[t_s^c]$, and the classical velocity is obtained by propagation in real time and space:

$$\mathbf{v}^C(t) = \mathbf{v}_\mathbf{k}(t) + \int_{t}^{T} dt\ \nabla U(\Re[\mathbf{r}_L^s(t)]). \quad (12)$$

To specify how the Coulomb potential leads to coupling between the real and the imaginary parts of the A*R*M trajectory and how neglecting the imaginary part of the exit coordinate we remove this coupling, consider the analytical continuation of the Coulomb potential to the complex plane. The procedure has been described in detail in [65]. Here we recall the results to make the discussion more specific. For a real vector $\mathbf{r}$, we have $U(\mathbf{r}) = -Z/\sqrt{\mathbf{r}\cdot\mathbf{r}}$. For a complex vector, $\mathbf{r} + i\boldsymbol{\rho}$, we have

$$U(\mathbf{r} + \mathbf{i}\boldsymbol{\rho}) = \frac{-Z}{\sqrt{(\mathbf{r} + i\boldsymbol{\rho})\cdot(\mathbf{r} + i\boldsymbol{\rho})}} = \frac{-Z}{\sqrt{r^2 - \rho^2 + 2i\mathbf{r}\cdot\boldsymbol{\rho}}}, \tag{13}$$

where $r = |\mathbf{r}|^2$ and $\rho = |\boldsymbol{\rho}|^2$. We choose the branch cut of the complex square root to be infinitesimally above the negative real axis to ensure that our contour never crosses the branch cut. The real and imaginary parts of the Coulomb potential are:

$$U = -\frac{Z}{\sqrt{2(a^2 + b^2)}}\left(\sqrt{\sqrt{a^2 + b^2} + a} - i\ \mathrm{sgn}(b)\sqrt{\sqrt{a^2 + b^2} - a}\right), \tag{14}$$

where

$$a = r^2 - \rho^2 \quad \text{and} \quad b = 2\mathbf{r}\cdot\boldsymbol{\rho}, \tag{15}$$

and

$$\mathrm{sgn}(b) = \begin{cases} -1, & \text{for } b \leqslant 0 \\ +1, & \text{for } b > 0. \end{cases} \tag{16}$$

The real and imaginary parts of the Coulomb force $\mathbf{F}_C(t) = -Z\mathbf{r}_L(t)/r_L^3(t)$:

$$\mathbf{F}_C(t) = -\nabla U(\mathbf{r} = \mathbf{r} + i\boldsymbol{\rho}) = -Z\frac{\mathbf{r} + i\boldsymbol{\rho}}{\|\mathbf{r} + i\boldsymbol{\rho}\|^3} \tag{17}$$

$$= -\frac{Z(\mathbf{r} + i\boldsymbol{\rho})}{[2(a^2 + b^2)]^3}\left([\sqrt{a^2 + b^2} + a]^{3/2} - 3b\sqrt{\sqrt{a^2 + b^2} - a}\right) \tag{18}$$

$$- i\,\mathrm{sgn}(b)\{3b\sqrt{\sqrt{a^2 + b^2} + a} - [\sqrt{a^2 + b^2} - a]^{3/2}\}), \tag{19}$$

describe the evolution of the real and imaginary parts of quantum trajectory $\mathbf{r}^Q(t)$.

Separating real and imaginary contributions to Coulomb force $\mathbf{F}_C$, we get:

$$\mathbf{F}_C = -\frac{Z}{[2(a^2 + b^2)]^3}[([\sqrt{a^2 + b^2} + a]^{3/2} - 3b\sqrt{\sqrt{a^2 + b^2} - a})\mathbf{r} + \tag{20}$$

$$\boldsymbol{\rho}\,\mathrm{sgn}(b)(3b\sqrt{\sqrt{a^2 + b^2} + a} - [\sqrt{a^2 + b^2} - a]^{3/2}) - \tag{21}$$

$$i\,\mathrm{sgn}(b)\{(3b\sqrt{\sqrt{a^2 + b^2} + a} - [\sqrt{a^2 + b^2} - a]^{3/2})\mathbf{r} - \tag{22}$$

$$\boldsymbol{\rho}([\sqrt{a^2 + b^2} + a]^{3/2} - 3b\sqrt{\sqrt{a^2 + b^2} - a})\}], \tag{23}$$

and we see the contribution of $\boldsymbol{\rho}(t)$ and $b(t)\mathbf{r}(t)$ to the real part of quantum velocity.

The coupling between the real and the imaginary parts of the A*R*M trajectory due to the Coulomb force is obvious. Even though the imaginary part of the A*R*M trajectory is constant after the barrier exit, the real part evolves and therefore both b and a are the functions of time along the A*R*M trajectory. Thus, the evolution in real time is affected by the presence of the imaginary exit coordinate. Depending on the sign of the parameter $b(t) = 2\mathbf{r}(t)\cdot\boldsymbol{\rho}(t)$, the Coulomb force either increases or decreases in its attractive strength.

The imaginary exit coordinate is present in quantum trajectory, but absent in the classical trajectory. This mismatch leads to the off-set in their real velocities at the exit point. The presence of the imaginary component of the A*R*M trajectory is due to the non-adiabaticity of the electron dynamics. Thus, in circularly polarised fields the majority of electrons released from *s*-orbitals will follow the classical trajectory (classical and quantum trajectories coincide in this case), but the majority of co- and counter-rotating electrons (released from the orbitals with $m \neq 0$) will follow quantum trajectories with non-zero imaginary parts. In this case, the degree of approximation that classical trajectory offers depends on the degree of non-adiabaticity of electron dynamics. We will illustrate this general picture below.

3. Results

We first consider the real parts of coordinates and velocities along the quantum trajectories at the 'exit time' $t = \Re[t_s^c] \equiv t_i^c$.

The parallel and perpendicular components of the coordinate or the velocity vector are defined w.r.t. the electric field. For velocity, these components $v_\parallel$ and $v_\perp$ are:

$$v_\parallel = \mathbf{v}_\mathbf{k}^c(t_i^c)\cdot\hat{\mathbf{E}}_\parallel(t_i^c), \tag{24}$$

$$v_\perp = \mathbf{v}_\mathbf{k}^c(t_i^c)\cdot\hat{\mathbf{E}}_\perp(t_i^c), \tag{25}$$

where $\hat{\mathbf{E}}_\parallel(t_i^c)$ and $\hat{\mathbf{E}}_\perp(t_i^c)$ are unit vectors parallel and perpendicular to the electric field, respectively, at the Coulomb-corrected time of exit $t_i^c = t_i + \Delta t_i^c$ (the real part of the saddle point, $t_i^c = \Re[t_s^c]$). The quantity $\hat{\mathbf{E}}_\perp(t_i^c)$ is positive if it has positive projection on the direction of the vector potential at the same time. For SFA, the time instants used are t_i.

3.1. Circularly polarised fields

We first consider a few-cycle, circularly polarised laser pulse, defined via its vector potential:

$$\mathbf{A}(t) = -\mathcal{A}_0 f(\omega t)(\cos\omega t\ \hat{\mathbf{x}} + \sin\omega t\ \hat{\mathbf{y}}), \tag{26}$$

where $\mathcal{A}_0$ is the amplitude. The envelope profile used here is $f(\omega t) = \cos^4(\omega t/2N_e)$ with $N_e = 2$. The peak field strength is defined as $\mathcal{E}_0 = \mathcal{A}_0\omega$. The most dominant ionisation event happens near $t = 0$, which maps onto a peak at $\phi_k = 0$ in the SFA theory. Long-range interactions lead to an offset in this

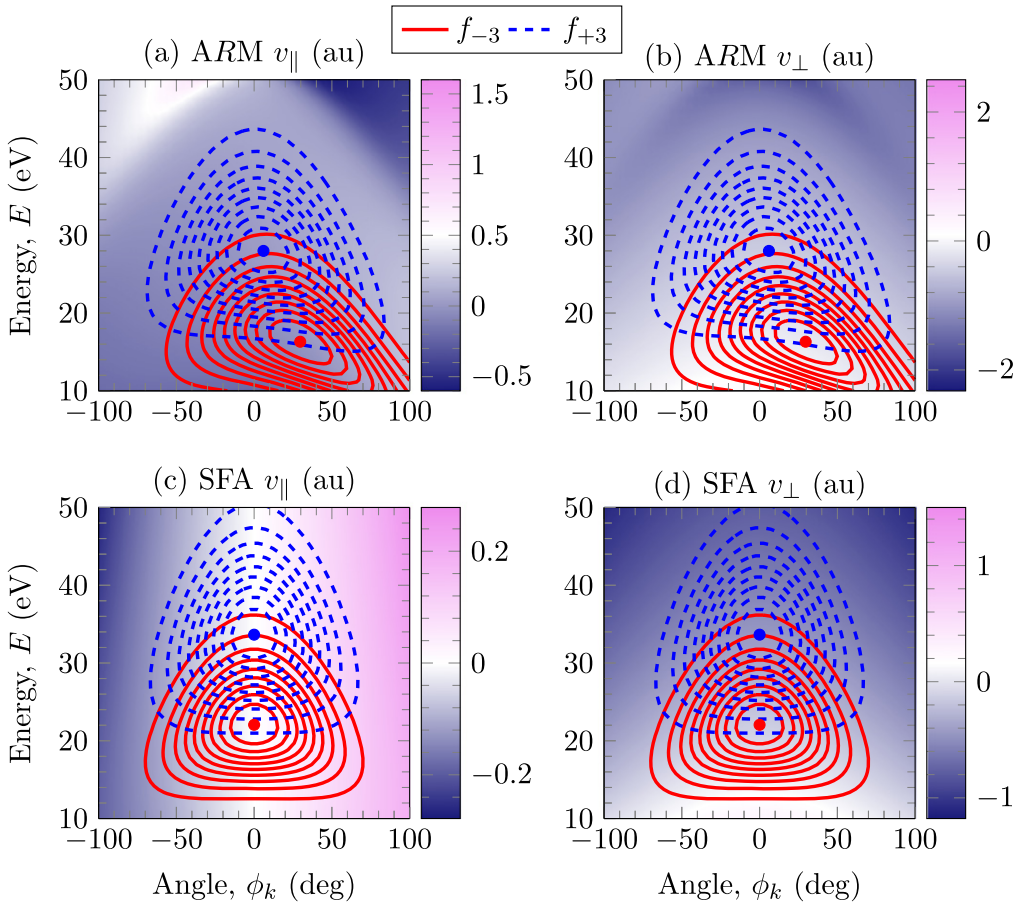

Figure 1. Distribution of exit velocities at the time instant $t = t_i^c$, for Yb III, at $\mathcal{E}_0 = 0.065$ au, $\lambda = 800$ nm, right circular polarised field. The outermost contour level corresponds to 10% electron population, the innermost to 90% electron population. For SFA, $\Delta \mathbf{v}^c(t) = 0$, and exit point is at SFA $t_i = \Re[t_s]$. Only real part of exit velocity, corresponding to quantum trajectory is shown.

mapping between the ionisation time and the momentum peak, which A*R*M accurately predicts for *s*-orbitals [66, 70]. The off-set angle is equal to $\omega\Re[t_s^c]$ [66, 70].

The velocities at the exit point (time $t = \Re[t_s^c] = t_i^c$) are shown in figure 1, as a function of the final (detected) energy and angle of the photoelectron. We use the example of Yb III, interacting with $\mathcal{E}_0 = 0.065$ au, $\lambda = 800$ nm, right circular polarised field. Superimposed on these distributions are the contour levels of the final photoelectron momentum distribution at the detector. Red solid curves are for f_{-3} (counter-rotating) orbital, which has the highest ionisation rate in a right-circularly polarised field. The blue dashed contours are for the f_{+3} (co-rotating) orbital, which has weaker photoelectron signal (see the companion paper I). Contours for both ARM (upper rows) and SFA (lower rows) are shown.

We begin with the analysis of the SFA results, see figure 1 (SFA, $v_{\perp}$, SFA $v_{\parallel}$). The velocity $v_{\perp}$ orthogonal to the instantaneous field at the time of exit is known to define the final energy of the photoelectron at the peak of the distribution (see e.g. [72]). Let us follow the contours, which specify the angle and energy dependence of co- and counter-rotating electrons, superimposed on the colour-coded background representing the 'exit' value of $v_{\perp}$ as a function of the final angle and energy of the photoelectron (see figure 1(d)). In agreement with our expectations, we find larger $v_{\perp}$ for the co-rotating electron at the peak of its momentum distribution, than for the counter-rotating electron at the peak of its momentum distribution. This non-adiabatic effect is discussed e.g. in [72]. It is responsible for the fact that counter-rotating electron (blue dashed contour) has the peak of its distribution at higher energy than the co-rotating electron (red solid contour). In the quasistatic limit, the perpendicular 'exit' velocity $v_{\perp}$ for both co- and counter-rotating electrons tends to zero, removing the difference between their spectra and ionisation rates.

The longitudinal 'exit' SFA velocity $v_{\parallel}$ (see figure 1(c)) varies as a function of the detection angle. It is zero for zero detection angle (where the maxima of both photoelecton distributions are located) and is exactly opposite for positive and negative angles. For positive detection angles, it is directed away from the core, while for negative detection angles, it is directed towards the core. This angular dependence reflects the non-adiababticity of electron dynamics due to the fast change of the magnitude of the laser field in the short pulse. In this respect, the situation becomes similar to linearly polarised fields, where non-adiabaticity of the electron response maps into non-zero longitudinal velocity for all ionisation times within the optical cycle, except for the ionisation time at the peak of the laser field.

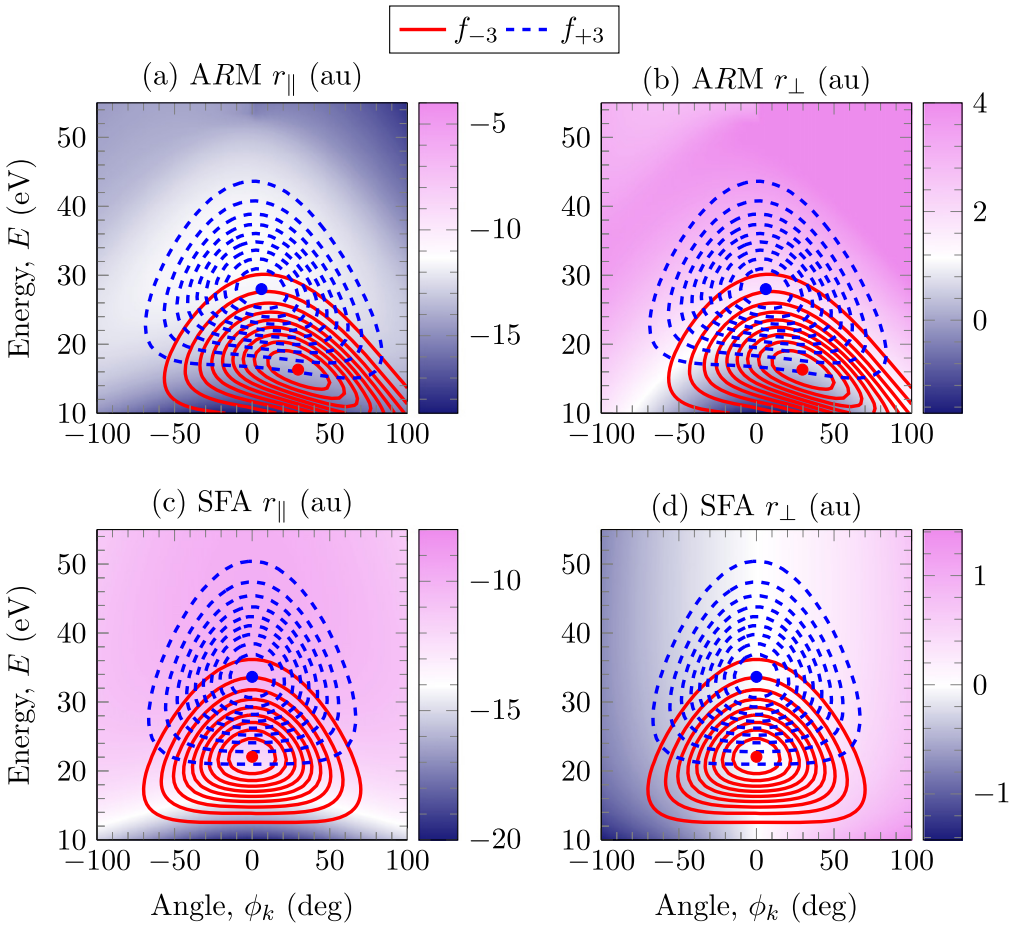

Figure 2. Distribution of exit coordinates at the 'exit time' $t = t_i^c$, for Yb III, at $\mathcal{E}_0 = 0.065$ au, $\lambda = 800$ nm, right circular polarised field. The outermost contour level corresponds to 10% electron population, the innermost to 90% electron population. For SFA, $\Delta\mathbf{v}^c(t) = 0$, and exit point is at SFA $t_i = \Re[t_s]$. Only real part of exit coordinate corresponding to the quantum trajectory is shown.

This (envelope-related) non-adiabatic feature of the 'exit' value of $v_{\parallel}$ already tells us that when the Coulomb potential is included, the trajectories with the SFA velocities directed towards the core can be more efficiently decelerated by the Coulomb field (and may even be trapped), than the trajectories with the SFA velocities directed away from the core. As a result, it is clear that when the Coulomb field is included, the final distributions will be more distorted (with respect to their SFA counterparts) for positive angles and less distorted for the negative angles. This is exactly what we see in figure 1(a), where the final momentum distributions are shown. They are superimposed on top of the colour-coded 'exit' velocities.

Overall, the main effect of the Coulomb potential is to 'skew' the final and the initial momentum distributions while mostly preserving the range of the 'exit' velocities arising in the short-range potential. This observation is in agreement with the standard assumptions of the Coulomb-corrected three-step models.

The range of variation of the transverse velocity component is reduced in A*R*M, compared to SFA, but is shifted to larger positive velocities. This is the influence of $\Delta\mathbf{v}^c(t_i)$. The SFA transverse velocity sharply depends on energy, whereas the A*R*M velocity spreads out gradually. Long-range interactions therefore lead to bunching of the trajectories just after emerging into the continuum.

We next consider initial coordinate distribution at the barrier exit, figure 2, where the coordinates parallel and perpendicular to the electric field direction are shown. These values of the exit coordinates correspond to quantum trajectories. In both SFA and A*R*M case, counter-rotating (f_{-3}) electrons have smaller parallel component of the coordinate than the co-rotating electron (f_{+3}) (figures 2(a) and (c)). Compare this to the perpendicular coordinate distribution (figures 2(b) and (d)): counter-rotating electrons are liberated farther from the core in terms of their perpendicular displacement, than the co-rotating electrons.

The extent of the parallel displacement is much stronger than perpendicular displacement, and thus, overall, the co-rotating electrons are liberated at a larger distance from the core than the counter-rotating electrons.

With this information on initial velocity and coordinates, we can develop a schematic of electron trajectories after tunnelling through the barrier.

The corresponding SFA quantum orbits and long-range quantum and classical trajectories for majority of electrons are shown in figure 3, for the time duration corresponding to two cycles of the laser field after ionisation (the laser field

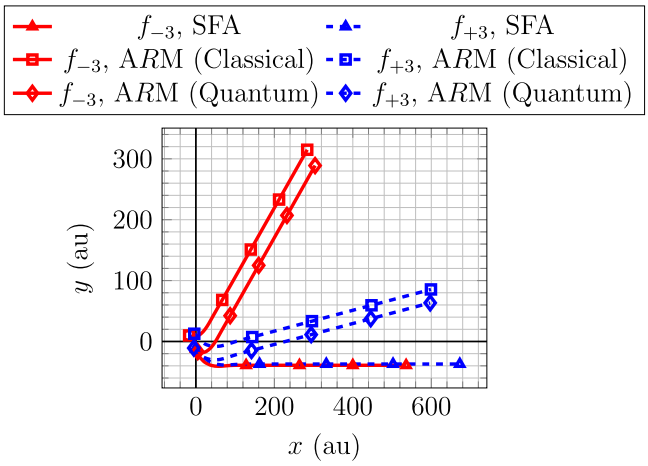

Figure 3. Real part of quantum orbits in SFA (curves with triangles), classical (curves with squares) and quantum (curves with diamonds) trajectories derived using ARM, for f_{-3} (solid curves) and f_{+3} (dashed curves) of Yb III, in a circularly polarised field. We see the sharp steering of electrons, with f_{-3} electrons experiencing strong counter-clockwise 'streaking' compared to f_{+3} electrons, in long-range potential. The real quantum trajectories differ from classical trajectories, because the dynamics of the majority of co- and counter-rotating electrons is manifestly non-adiabatic.

switches off after one cycle). The curve with red solid triangles represents the SFA trajectory for f_{-3} orbital and the curve with the blue dashed triangles is the SFA trajectory for the f_{+3} orbital. The two trajectories are very close to each other, with f_{+3} ending up slightly farther from f_{-3}, due to its higher momentum, as expected.

When the long-range Coulomb interaction is switched on, however, we see a significant difference between the trajectories for the f_{-3} and f_{+3} electrons, travelling in very different directions (as one would expect from the full picture [71]). While the f_{+3} electrons still maintain greater distance from the core than their f_{-3} counterparts, the f_{-3} electrons show larger steering by the laser field compared to f_{+3} electrons.

This leads to larger offset angle in the photoelectron spectra at the detector [71]. The SFA trajectories fail to capture this essential feature.

As discussed in detail in section 2.3, we can either define the real initial conditions at the barrier exit (real part of coordinate on quantum trajectory at the exit time, real velocity obtained by back propagation from the final momentum **k** to real exit coordinate, see equations (11) and (12)) and then propagate them to the detector in real time, leading to the curve with with squares in figure 3(a) (classical), or we can perform propagation directly from the 'entrance to the barrier' (in complex space and time), guided by the matching scheme and leading to the quantum trajectories (equations (9) and (10)). The difference between the two after the exit point is due to imaginary exit coordinate missing in classical trajectory and present in the quantum trajectory and is a result of the coupling between the real and imaginary components of the quantum trajectories.

The coupling can be understood by considering the Coulomb force (see section 2.3) on the imaginary trajectory. Its real part depends on the parameter $b(t)$, proportional to the imaginary part of the exit coordinate:

$$b(t) = 2\left(-k\tau_s + \frac{A_0}{\omega}\sinh\omega\tau_s\right)\left(kt - \frac{A_0}{\omega}\sin\omega t\right), \qquad (27)$$

for any real $t \geqslant t_{exit}$, τ_s is the imaginary part of complex SFA ionisation time t_s.

For circularly polarised fields $\left(-k\tau_s + \frac{A_0}{\omega}\sinh\omega\tau_s\right) = 0$ (hence $b(t) = 0$) at optimal momentum, corresponding to the majority of s-electrons. However, the spectral peaks corresponding to co- and counter-rotating electrons are on the opposite sides from the peak of photoelectron spectrum for s-electrons. Thus, $b > 0$ for counter- and $b < 0$ for co-rotating electron, reflecting the fact that these electrons are not born at the peak of the laser field, i.e. their dynamics is manifestly non-adiabatic. The deviation between the classical and the real part of the quantum trajectories in the long-range potential is due to this effect.

In elliptical fields $b \neq 0$ for s-orbitals and therefore co- and counter-rotating electrons are 'asymmetrically' off-set from $b = 0$. In this case the degree of mismatch between the classical and quantum trajectories in long-range potential depends on the magnetic number m of the orbital (i.e., whether it is co-rotating or counter-rotating w.r.t. the field).

3.2. Elliptically polarised fields

Non-adiabaticity of ionisation is the key reason for the deviations between the classical and quantum trajectories. It is enhanced due to the application of short pulses, Coulomb-laser coupling and is, probably, best detected by looking at orbitals with large l, m. However, the ellipticity of the field offers an additional control knob: non-adiabaticity of ionisation is also enhanced by decreasing the ellipticity, because the sub-cycle variation of the field comes into play. It is particularly relevant for long pulses, where the ionisation dynamics in circularly polarised fields becomes largely adiabatic. Analysing the initial conditions for various orbitals, the differences in the evolution of quantum and classical trajectories we can clearly identify the 'degree' of non-adiabaticity of strong field ionisation. We will now focus on orbitals with lower m, l, such as s and p orbitals and longer laser pulses. As discussed earlier, $b(t) \neq 0$ already for the majority of s electrons in elliptical fields, leading to m-dependent deviations between classical and quantum trajectories for $\$l \geq 1\$$, which we illustrate here.

We extend the method we recently employed in [73], to include initial coordinate with Coulomb corrections due to the under the barrier dynamics.

We consider elliptically polarised short pulse with the vector potential defined as:

$$\mathbf{A}(t) = A_0 f(t)[\cos(\omega t + \phi_{\mathrm{CEP}})\hat{\mathbf{x}} + \varepsilon\sin(\omega t + \phi_{\mathrm{CEP}})\hat{\mathbf{y}}], \qquad (28)$$

$$\text{with envelope, } f(t) = \cos^2\left(\frac{\omega t}{2N_e}\right). \qquad (29)$$

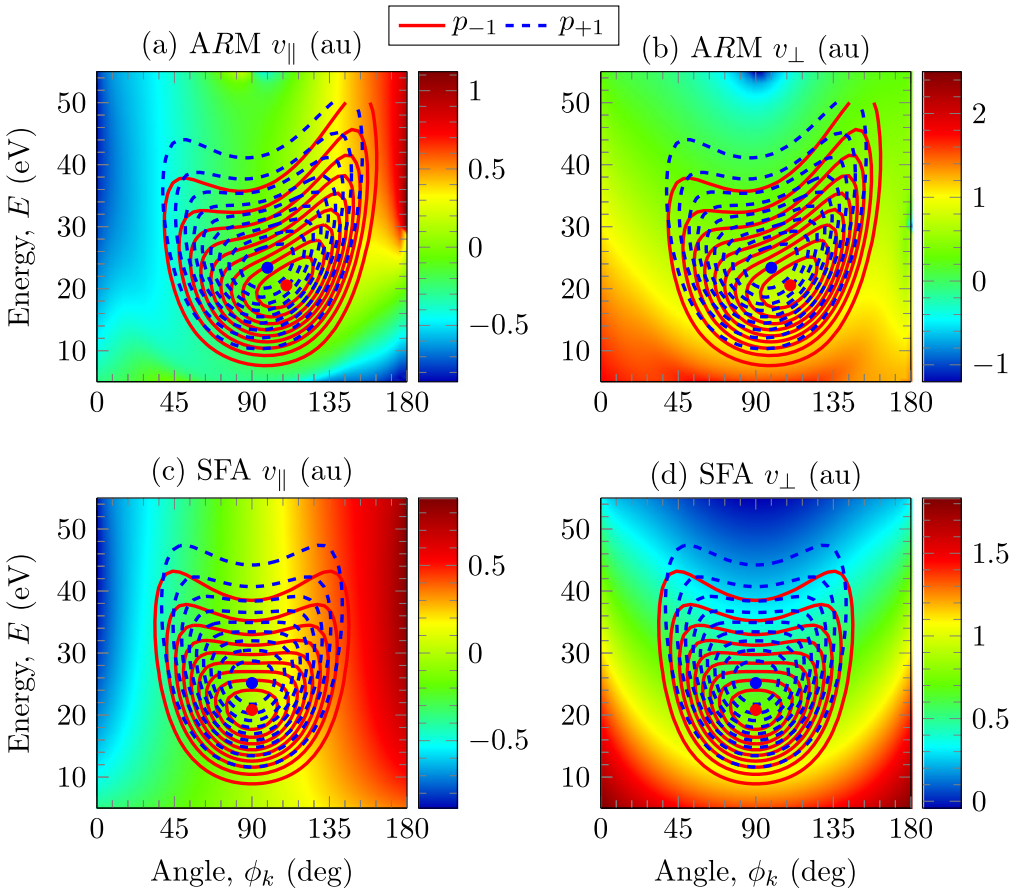

Figure 4. Distribution of exit velocity (the real part of velocity on quantum trajectory) at time instant $t = \Re[t_s^c]$ ($t = \Re[t_s]$ for SFA case), for Ar II, with field parameters: $\mathcal{E}_0 = 0.115$ au, $\lambda = 780$ nm, $\varepsilon = 0.61$, right-elliptically polarised field.

Here we choose $\mathcal{E}_0 = 0.115$ au, $\lambda = 780$ nm, $\varepsilon = 0.61$, $\phi_{\rm CEP} = 3\pi/2$, and $N_e = 6$ cycles. For Ar II, the ionisation potential is $I_p = 27.630$ eV.

The electric field defined from the vector potential of equation (29) has its major axis along the x-axis, which means that the peak of the photoelectron distribution is close to the y-axis, as is also evident from the contour plots in figures 4 and 5. The symmetry breaking around $\phi_k = 90°$ is the well-known effect of the Coulomb interaction [74, 75].

3.3. Initial conditions versus ellipticity

Figure 6 shows the perpendicular and parallel components of the exit coordinate and velocity (real parts of quantum trajectories and their respective velocities at the exit time), respectively, as a function of ellipticity for the majority of p^- and p^+ electrons liberated from Ar II.

Brief analysis shows that the parallel displacement of p^- electron is always higher than that of p^+ electrons. Counter-rotating electrons also have higher perpendicular and parallel exit velocity (figure 6(b)). This is in contrast to circular fields, where parallel displacement for p^+ electrons is higher than for the p^- electrons.

The result for exit parallel velocities shown in figure 6 is particularly instructive. The parallel velocity is zero in short-range potential in the adiabatic regime, it always applies to the majority of electrons in SFA. Figure 6 shows that in long-range potentials, the parallel velocity for the majority of the p^+ and p^- electrons is small, but not equal to zero. The non-zero velocity is due to the non-adiabaticity of electron dynamics and subsequent sub-barrier Coulomb-laser coupling. Note that the respective result for the majority of s electrons (with the same I_p) would be squeezed in between the green and black curves for p^+ and p^- electrons. First, we see that for elliptically polarised fields and ellipticity in the range $\varepsilon \simeq 0.4$–0.8, co-rotating p^+ electrons have the largest non-zero initial velocities, i.e. they are the most non-adiabatic in elliptical fields. The s-electrons follow next and then, the most 'adiabatic' in elliptical fields are the p^- electrons. In contrast, recall that in circularly polarised fields, the most adiabatic are the s-electrons. Indeed, for ellipticity $\varepsilon = 1$, the exit parallel velocity is very close to zero for s and p^- electrons, because the pulse we are using (for given frequency and intensity) is already sufficiently long to significantly suppress the non-adiabaticity of ionisation along the major field axis for the majority of s and p^- electrons in circularly polarised fields, but not for p^+ electrons. Just like in short-range potential, the non-zero parallel exit velocity reflects non-adiabaticity of ionisation dynamics in long-range potentials and the parallel velocity is equal to zero in the adiabatic limit. In adiabatic (long-wavelength) limit the ARM predictions for the photo-electron angular and energy distributions in attoclock set-up

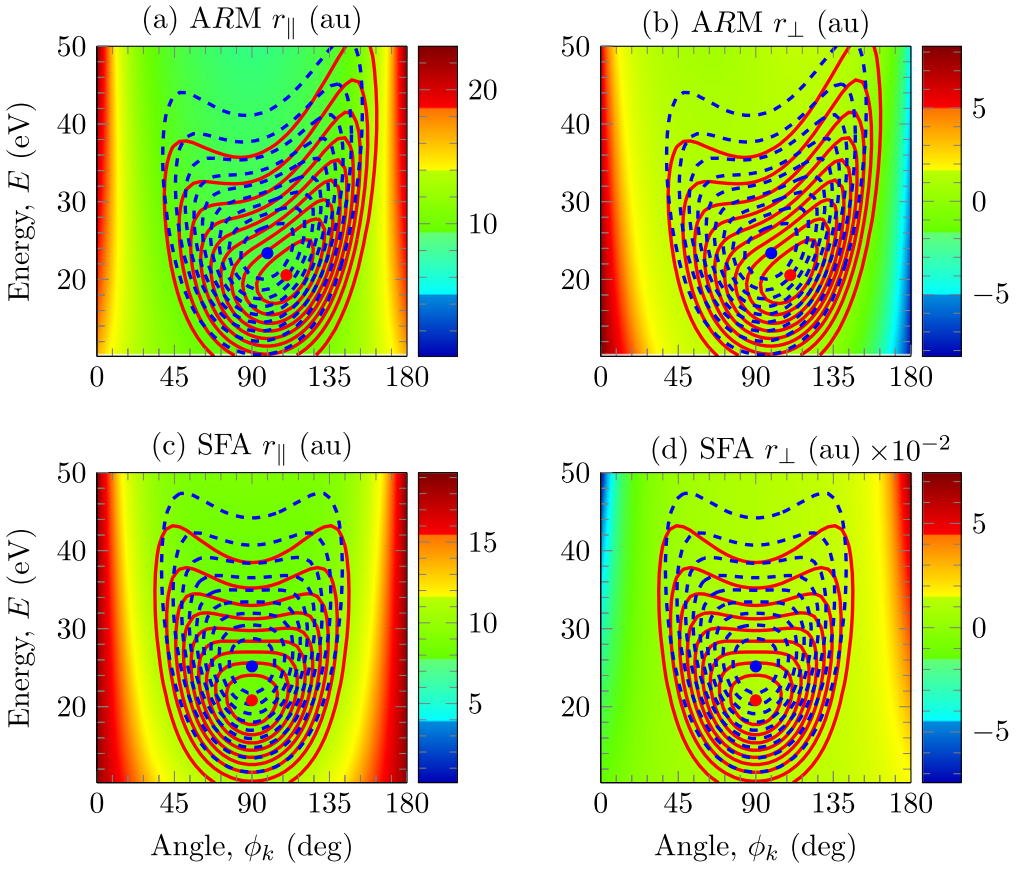

Figure 5. Distribution of exit coordinate (the real part of quantum trajectory) at time instant $t = \Re[t_s^c]$ ($t = \Re[t_s]$ for SFA case), for Ar II, with field parameters: $\mathcal{E}_0 = 0.115$ au, $\lambda = 780$ nm, $\varepsilon = 0.61$, right-elliptically polarised field.

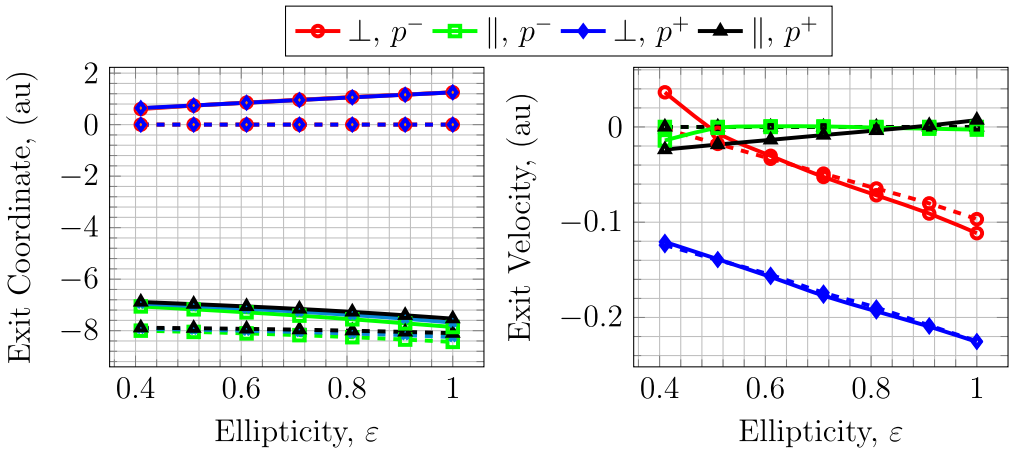

Figure 6. Exit parallel and perpendicular (a) coordinate and (b) velocity, for p^- and p^+ electrons of Ar II, at effective field strength $\mathcal{E}_0 = 0.115$ au, $\lambda = 780$ nm, six-cycle, right-polarised elliptical field, real parts of quantum trajectories (solid) in long-range potential and (dashed) in short-range potential (SFA).

(strong field ionisation in circularly polarised fields) are remarkably accurate [70], further supporting our conclusions.

In figure 8, we show the (a) real and (b) imaginary parts of the trajectories corresponding to the peak of the photoelectron spectra for the p^- and p^+ electrons, for $\varepsilon = 0.61$, for the SFA (triangles), classical (squares) and quantum (diamond) trajectories in the long-range potential. We take into account the impact of the Coulomb momentum shift term $\Delta \mathbf{v}^c(t)$ for the A*R*M quantum orbits. The difference between the SFA and the A*R*M trajectories is the deflection of the trajectories in the long-range potential. The effect depends on the magnetic number m of the initial bound state: counter-rotating electrons (p^-) experience greater deflection by the Coulomb potential compared to the co-rotating (p^+) electrons. Both p^- and p^+ electrons emerge from under the barrier at almost the same point in space, but p^- electrons are released after the peak of the pulse (see Figure 7) and are more likely to pass closer to the core (see Figure 8). We can also see some

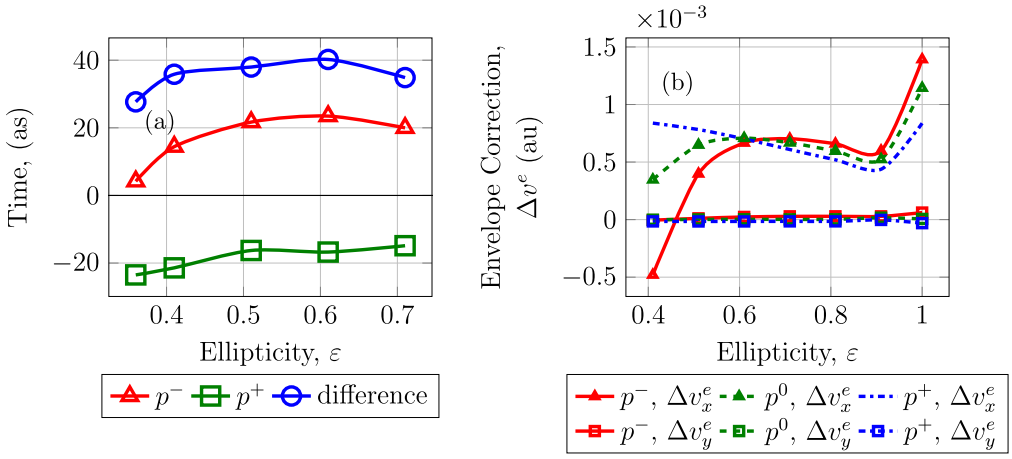

Figure 7. (a) Timing information of most probably p^- and p^+ electrons, as a function of ellipticity. Red solid line is the most probable release time for p^- electrons, green dashed for the p^+ electrons, and blue dotted line is the difference between the two. There is a general trend of the increasing time delay between p^- and p^+ electrons, with increasing ellipticity. (b) Envelope effects and associated corrections for nearly single-cycle pulses, for p^-, p^0, and p^+ orbitals, as a function of ellipticity. The effects are negligible, on the scale of 10^{-3} au. Field parameters: $\lambda = 780$ nm, $\cos^2$-envelope, six-cycle, right-elliptically polarised field.

difference between the A*R*M quantum trajectories and A*R*M classical trajectories, especially for the p^+ orbital (blue dashed curves in figure 8) discussed above.

4. Adiabatic expressions

Before concluding this paper, we present simple, analytical expressions for the Coulomb momentum shift $\Delta\mathbf{v}^c$, which is essential for describing the enhancement in ionisation of the counter-rotating versus the co-rotating electrons. We consider the adiabatic regime $\gamma \ll 1$.

Let the electric field point along the positive y-axis during the instant of ionisation, leading to the electrons drifting in the positive x-direction in the continuum. The Coulomb potential yields the correction $\Delta v_\parallel^c$ to velocity parallel to the electric field, and $\Delta v_\perp^c$ to the velocity perpendicular to the electric field.

We assume $\mathcal{E}_0 \ll \mathcal{E}_{\rm at}$ (where $\mathcal{E}_{\rm at} = \kappa^3$ is the atomic field strength) and $\gamma \ll 1$. For laser field strength pointing along (or near) y-axis as the electron escapes, we find the momentum shift to be defined, in the first order in Z, by the expression:

$$\Delta v_y^c \equiv \Delta v_\parallel^c = \frac{\pi Z\mathcal{E}_0}{\kappa^3} + i\frac{Z\mathcal{E}_0}{\kappa^3}\left(\frac{1}{2} + \ln\frac{Q\mathcal{E}_0}{2\kappa^4} + \frac{3}{4}\frac{Q\mathcal{E}_0}{\kappa^4}\right), \quad \gamma \ll 1. \tag{30}$$

This is the approximate expression for momentum shift in the direction of the field at the instant of ionisation. The real part of this expression is equivalent to the adiabatic momentum shift outside of the barrier given by equation (78) of [64], because in the adiabatic regime, there is no sub-barrier contribution to the real Coulomb shift. The momentum shift perpendicular to the field is zero in $\mathcal{O}(\gamma)$, becasue it is manifestly non-adiabatic. thus, we need to expand to higher order in the Keldysh parameter γ

$$\Delta v_x^c \equiv \Delta v_\perp^c = \frac{Z\omega}{4\kappa^2}\left(\frac{1}{6} + \ln\frac{Q\mathcal{E}_0}{2\kappa^4} + \frac{2}{3}\frac{Q\mathcal{E}_0}{\kappa^4}\right) - i\frac{\pi Z\omega}{4\kappa^2}, \tag{31}$$

Figure 9 compares these approximate expressions with exact result equation (5). The agreement is excellent for $\Delta v_\parallel^c$, because it is 'less non-adiabatic' than $\Delta v_\perp^c$ (figures 9(a) and (b)). We also note that, even though equation (30) is supposed to be valid for $\gamma \ll 1$, we get very good agreement for $\gamma \simeq 4$, well into the non-adiabatic limit. The velocity in orthogonal direction is as non-adiabatic as it gets and one should use even more terms in the expansion w.r.t. γ to converge to $\Delta v_\perp^c$ given by equation (5). However, we have found that even at the current level of approximation for velocities, the approximate expression for ionisation rates has a reasonable quality (see Figure 9).

Indeed, for $\ell \neq 0$, and adiabatic case, we have:

$$\Delta t_s^c = -\frac{\mathbf{v_k}(t_s)\cdot\Delta\mathbf{v}^c}{\mathbf{v_k}(t_s)\cdot\mathbf{E}(t_s)} \approx \frac{i(\gamma\Delta v_\perp^c/2 + i\Delta v_\parallel^c)}{\mathcal{E}_0}. \tag{32}$$

Even though $\gamma \ll 1$, and $\Delta v_\perp^c \ll \Delta v_\parallel^c$ (figure 9), we still need to keep $\gamma\Delta v_\perp^c$, as shown below.

We can now calculate the complex deviation angle $\Delta\alpha_{\chi k}^c$ (equation (A.7) in [71]):

$$\Delta\alpha_{\chi k}^c(t) = \arctan\Lambda \equiv \arctan\frac{\|\mathbf{E}(t_s)\Delta t_s^c + \Delta\mathbf{v}^c(t)\|}{v_{\mathbf{k}}(t_s)} \approx \frac{\Delta v_\perp^c + i\gamma\Delta v_\parallel^c}{i\kappa}. \tag{33}$$

We find that $\Delta v_\perp^c$ and $\gamma\Delta v_\parallel^c$ are on par.

The Coulomb complex angle shift $\Delta\alpha_{\chi k}^c$ enters expressions for the quantum amplitudes via $\exp(-im\Delta\alpha_{\chi k}^c)$. Therefore, it is the *real* part of the complex momentum shift $\Delta v_\perp^c$ and the imaginary part of $\Delta v_\parallel^c$, that define the ratio of the ionisation rates for the counter- and co-rotating electrons.

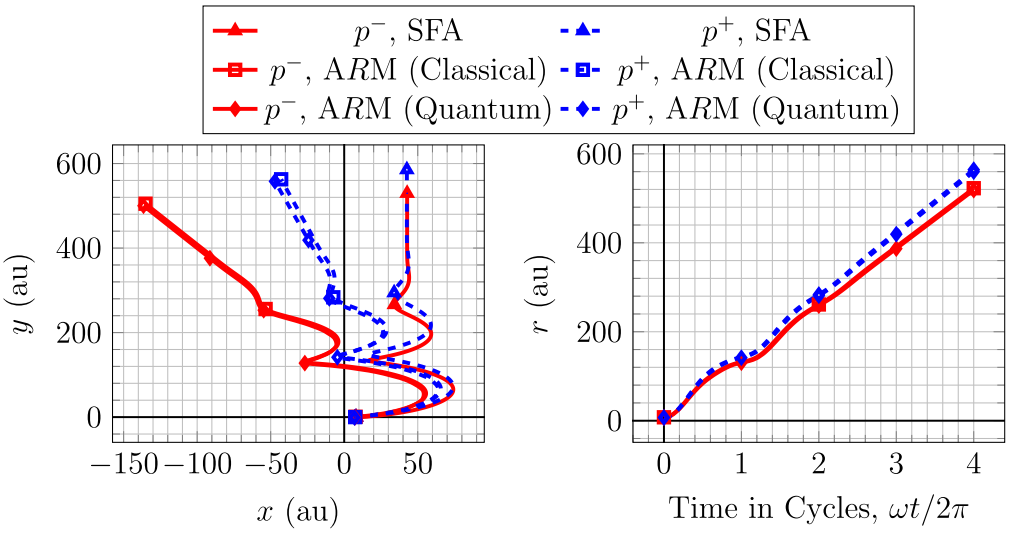

Figure 8. Comparison of SFA (triangles), classical (squares), and real part of quantum (diamonds) trajectories in long-range potential for (red solid) p^- and (blue dashed) p^+ electrons, at ellipticity $\varepsilon = 0.61$. Quantum trajectories deviate from the classical trajectories mostly for the p^+ orbitals. (b) Radial coordinate for the classical (squares) and quantum (diamonds) trajectories in the long-range potential, as a function of time, after the exit from the barrier. p^- electrons are liberated just after the peak of the pulse. They traverse closer to the core, leading to stronger interaction with the Coulomb potential. On the other hand, the p^+ electrons are released just before the peak, and interact weaker with the core.

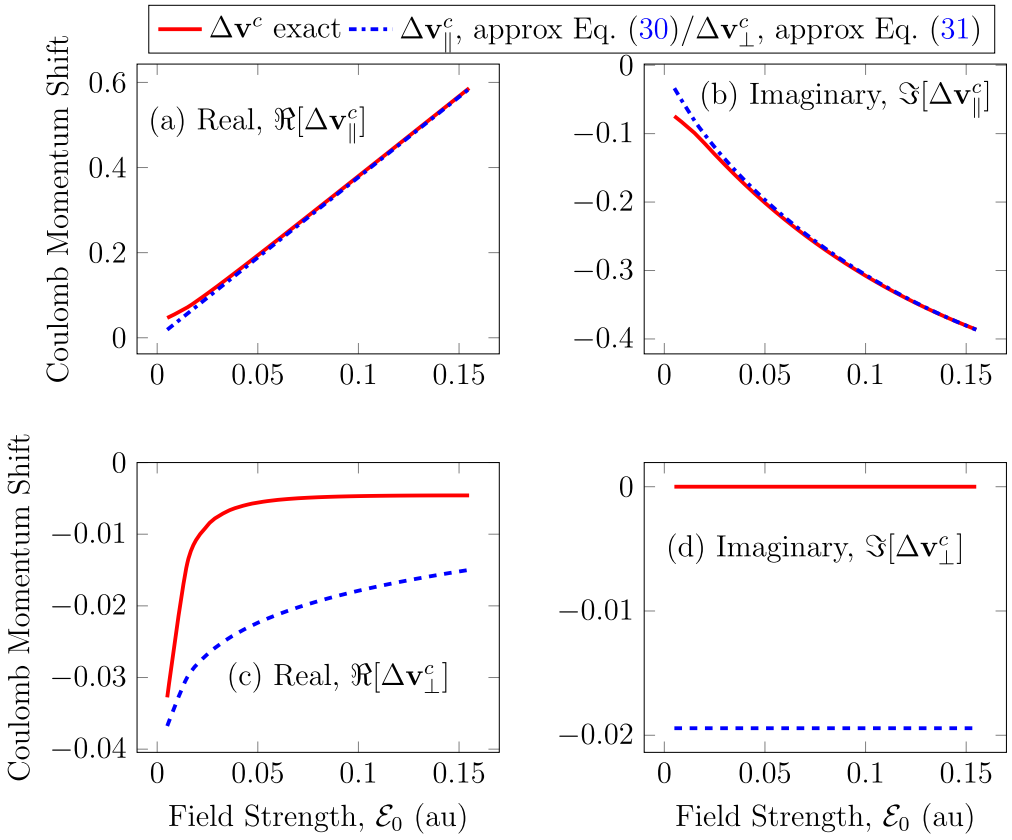

Figure 9. Comparison of exact expression for $\Delta\mathbf{v}^c$, with the approximate expressions (equations (30) for $\Delta v_\parallel^c$ and equation (31) for $\Delta v_\perp^c$), as function of field strength. The exact curves are shown in solid red, and approximate expressions are shown in blue dashed curves. We use Yb III, $Q = 3$, $I_p = 0.92$ au, with laser field parameters: $\lambda = 3$ μm, monochromatic circularly polarised field.

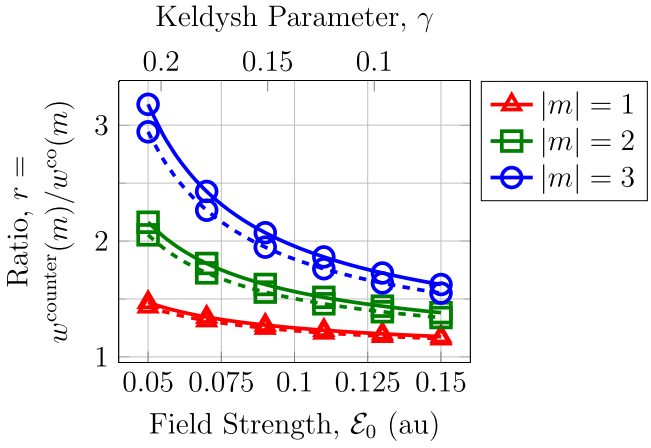

Figure 10. Comparison of exact (solid curves) and approximate (dashed curves) ratio (equation (37)) of counter- to co-rotating ionisation rates, for Yb III. Field parameters: $\lambda = 6\ \mu$m, monochromatic, right-circularly polarised field. We find very good agreement between exact and approximate results.

This is in line with expectations, as the bulk of the real part of $\Delta v_\perp^c$ and the imaginary part of $\Delta v_\parallel^c$ are mostly defined under the barrier.

The final expression for the ratio between counter- and co-rotating electrons rates, for $\gamma \ll 1$, is:

$$r \approx \exp\left[4|m|\coth^{-1}\frac{1}{\zeta_0}\sqrt{\frac{\zeta_0^2+\gamma^2}{1+\gamma^2}}\right] \times \exp\left[\frac{4|m|}{\kappa}(\Re[\Delta v_x] - \gamma\Im[\Delta v_y]\right], \gamma \ll 1,\ \mathcal{E}_0 \ll \kappa^3, \tag{34}$$

$$\Re[\Delta v_\perp^c] = \frac{Z\omega}{4\kappa^2}\left(\frac{1}{6} + \ln\frac{Q\mathcal{E}_0}{2\kappa^4} + \frac{2}{3}\frac{Q\mathcal{E}_0}{\kappa^4}\right), \tag{35}$$

$$\Im[\Delta v_\parallel^c] = \frac{Z\mathcal{E}_0}{\kappa^3}\left(\frac{1}{2} + \ln\frac{Q\mathcal{E}_0}{2\kappa^4} + \frac{3}{4}\frac{Q\mathcal{E}_0}{\kappa^4}\right), \tag{36}$$

where $\zeta_0 \approx \gamma^2/3$. The first exponential in equation (37) is the SFA ratio [72], while the second exponential is the additional m-specific contribution from the Coulomb potential, manifesting through the momentum shift $\Delta\mathbf{v}^c$ and time correction Δt_s^c. Further simplification gives us the compact expression:

$$r \approx \exp\left[4|m|\coth^{-1}\frac{1}{\zeta_0}\sqrt{\frac{\zeta_0^2+\gamma^2}{1+\gamma^2}}\right] \times \exp\left[\frac{-|m|Z\omega}{\kappa^3}\left(\frac{11}{6} + 3\ln\frac{Q\mathcal{E}_0}{2\kappa^4} + \frac{7}{3}\frac{Q\mathcal{E}_0}{\kappa^4}\right)\right]. \tag{37}$$

A comparison of this approximate ratio and the exact-A*R*M ratio is shown in figure 10, for Yb III, at $m = \pm 3$. The agreement gets better for lower m. Thus, the higher m, the more non-adiabatic terms need to be included. The overall agreement between the approximate A*R*M ratio equation (37) and the exact results is good. Deviation from the exact result is at most $\simeq$8% (for $|m| = 3$). Therefore, equation (37) can serve as a succinct formula for the ratio of the ionisation yields of the counter- to co-rotating electrons, in the long-range potentials in non-adiabatic domain.

5. Conclusion

We have applied the A*R*M theory to obtain electron velocities and coordinates at the exit from the tunnelling barrier in strong field ionisation by few-cycle circularly and elliptically polarised fields.

The opportunity to derive such initial conditions emerges as a corollary of analysing sub-barrier kinematics, i.e. the interplay of laser and Coulomb fields on the sub-cycle scale.

We have derived the quantum trajectories describing the electron dynamics in long-range potential and evolving in complex time and space. We have also derived their classical counterpart: the trajectories evolving in real time and real space in long-range potential. The difference between classical and quantum trajectories is proportional to the degree of non-adiabaticity of ionisation dynamics and related to fact that the ionisation process is not completed after the 'exit' from the barrier (see the companion paper and [65]). Despite this difference, the key features that characterise the difference in the final photoelectron distributions for the co- and counter-rotating electrons are reproduced by both quantum and classical trajectories corresponding to the majority of electrons. For example, the trajectories for the counter-rotating electrons experience larger deflection by the long-range Coulomb-type potential of the core. In particular, the classical trajectories corresponding to real initial conditions (real parts of velocities and coordinates taken at real value of the saddle point for time, all Coulomb-corrected) does not seem to betray our intuition in capturing the basic physics.

We have presented analytical expressions for the ratio of the counter- to co-rotating electron yields, in the adiabatic limit, obtaining very good agreement with the exact-A*R*M results. These analytical expressions can be tested in experiments and used as a a guide for understanding the orbital-specific Coulomb correction.

We also clarified the misconception in the literature that A*R*M assumes zero initial parallel velocity at the exit from the barrier [76]. We show that (i) A*R*M offers a rigorous framework for establishing quantum and classical trajectories reflecting ionisation dynamics in long-range potentials, (ii) the parallel velocity is different for different ellipticities and orbitals with different l, m and thus is often non-zero, (iii) the exit parallel velocity is zero in long-range potentials in the adiabatic limit. In this, long-wavelength, limit A*R*M predictions for photoelectron angular and energy distributions in the attoclock set-up (strong field ionisation in circularly polarised fields) are remarkably accurate [70], further supporting our conclusions.

Acknowledgments

OS gratefully acknowledges financial support from the EU ITN MEDEA-AMD-641789-17. JK and OS gratefully acknowledge financial support from the DFG grant SM 292/2-3.

ORCID iDs

Jivesh Kaushal https://orcid.org/0000-0002-3499-7553
Olga Smirnova https://orcid.org/0000-0002-7746-5733

References

[1] Lambropoulos P 1985 Mechanisms for multiple ionization of atoms by strong pulsed lasers *Phys. Rev. Lett.* **55** 2141
[2] Yergeau F, Chin S L and Lavigne P 1987 Multiple ionisation of rare-gas atoms by an intense CO_2 laser (10^{14} W cm^{-2}) *J. Phys. B: At. Mol. Phys.* **20** 723
[3] Normand D and Schmidt M 1996 Multiple ionization of atomic and molecular iodine in strong laser fields *Phys. Rev.* A **53** R1958
[4] Taïeb R, Véniard V and Maquet A 2001 Photoelectron spectra from multiple ionization of atoms in ultra-intense laser pulses *Phys. Rev. Lett.* **87** 053002
[5] Dörner R, Weber Th and Weckenbrock M 2003 Multiple ionization in strong laser fields *Adv. At. Mol. Opt. Phys.* **48** 1
[6] Lewenstein M *et al* 1994 Theory of high-harmonic generation by low-frequency laser fields *Phys. Rev.* A **49** 2117
[7] Gibson E A *et al* 2004 High-order harmonic generation up to 250 eV from highly ionized argon *Phys. Rev. Lett.* **92** 033001
[8] Seres J *et al* 2005 Laser technology: source of coherent kiloelectronvolt x-rays *Nature* **433** 596
[9] Levesque J *et al* 2007 High harmonic generation and the role of atomic orbital wave functions *Phys. Rev. Lett.* **98** 183903
[10] Mairesse Y *et al* 2010 High harmonic spectroscopy of multichannel dynamics in strong-field ionization *Phys. Rev. Lett.* **104** 213601
[11] Paulus G G, Nicklich W and Walther H 1994 Investigation of above-threshold ionization with femtosecond pulses: connection between plateau and angular distribution of the photoelectrons *Europhys. Lett.* **27** 267
[12] Paulus G G *et al* 1994 Plateau in above threshold ionization spectra *Phys. Rev. Lett.* **72** 2851
[13] Becker W, Lohr A and Kleber M 1994 Effects of rescattering on above-threshold ionization *J. Phys. B: At. Mol. Opt. Phys.* **27** L325
[14] Delone N B and Krainov V 2000 *Multiphoton Processes in Atoms* (*Springer Series on Atomic, Optical, and Plasma Physics*) vol 13 2nd edn (Berlin: Springer)
[15] Milošević D B and Ehlotzky F 1998 Influence of screening of the coulomb potential on the plateau in above-threshold ionization *Phys. Rev.* A **57** 5002
[16] Milošević D B, Bauer D and Becker W 2006 Quantum-orbit theory of high order atomic processes in intense laser fields *J. Mod. Opt.* **53** 125
[17] Spanner M, Smirnova O, Corkum P B and Ivanov M 2004 Reading diffraction images in strong field ionization of diatomic molecules *J. Phys. B: At. Mol. Opt. Phys.* **37** L243
[18] Chen Z, Le A-T, Morishita T and Lin C D 2009 Quantitative rescattering theory for laser-induced high-energy plateau photoelectron spectra *Phys. Rev.* A **79** 033409
[19] Xu J *et al* 2012 Laser-induced electron diffraction for probing rare gas atoms *Phys. Rev. Lett.* **109** 233002
[20] Pullen M G *et al* 2015 Imaging an aligned polyatomic molecule with laser-induced electron diffraction *Nat. Commun.* **6** 7262
[21] Huismans Y *et al* 2011 Time-resolved holography with photoelectrons *Science* **331** 61
[22] Song X, Lin C, Sheng Z, Chen Z, Liu P, Yang W, Hu S, Lin C D and Chen J 2016 Unraveling nonadiabatic ionization and coulomb potential effect in strong-field photoelectron holography *Sci. Rep.* **6** 28392
[23] Eckle P, Smolarski M, Schlup P, Biegert J, Staudte A, Schöffler M, Muller H G, Dörner R and Keller U 2008 Attosecond angular streaking *Nat. Phys.* **4** 565
[24] Eckle P, Pfeiffer A N, Cirelli C, Staudte A, Dörner R, Muller H G, Büttiker M and Keller U 2008 Attosecond ionization and tunneling delay time measurements in helium *Science* **322** 1525
[25] Itatatni J *et al* 2004 Tomographic imaging of molecular orbitals *Nature* **432** 867
[26] Lein M, Hay N, Velotta R, Marangos J P and Knight P L 2002 Interference effects in high-order harmonic generation with molecules *Phys. Rev.* A **66** 023805
[27] Kanai T, Minemoto S and Sakai H 2005 Quantum interference during high-order harmonic generation from aligned molecules *Nature* **435** 470
[28] Lein M 2007 Molecular imaging using recolliding electrons *J. Phys. B: At. Mol. Opt. Phys.* **40** R135
[29] Ivanov M, Brabec T and Burnett N 1996 Coulomb corrections and polarization effects in high-intensity high-harmonic emission *Phys. Rev.* A **54** 742
[30] Morishita T, Le A T, Chen Z and Lin C D 2008 Accurate retrieval of structural information from laser-induced photoelectron and high-order harmonic spectra by few-cycle laser pulses *Phys. Rev. Lett.* **100** 013903
[31] Smirnova O *et al* 2009 Strong-field control and spectroscopy of attosecond electron-hole dynamics in molecules *Proc. Natl. Acad. Sci. USA* **106** 16556
[32] Smirnova O, Mairesse Y, Patchkovskii S, Dudovich N, Villeneuve D, Corkum P and Ivanov M Y 2009 High harmonic interferometry of multi-electron dynamics in molecules *Nature* **460** 972
[33] Smirnova O, Patchkovskii S, Mairesse Y, Dudovich N, Villeneuve D, Corkum P and Ivanov M 2009 Attosecond circular dichroism spectroscopy of polyatomic molecules *Phys. Rev. Lett.* **102** 063601
[34] Haessler S *et al* 2010 Attosecond imaging of molecular electronic wavepackets *Nat. Phys.* **6** 200
[35] Haessler S, Caillat J and Salières P 2011 Self-probing of molecules with high harmonic generation *J. Phys. B: At. Mol. Opt. Phys.* **44** 203001
[36] Bruner B D *et al* 2016 Multidimensional high harmonic spectroscopy of polyatomic molecules: detecting sub-cycle laser-driven hole dynamics upon ionization in strong mid-ir laser fields *Faraday Discuss* **194** 369
[37] Sukiasyan Suren, Smirnova Olga , Brabec Thomas, Ivanov Misha Yu and Patchkovskii Serguei 2010 Exchange and polarization effect in high-order harmonic imaging of molecular structures **82** 043414
[38] Pedatzur O., Orenstein G., Serbinenko V., Soifer H., Bruner B. D., Uzan A.J., Brambila D. S., Harvey A. G., Torlina L., Morales F., Smirnova O. and Dudovich N. 2015 Attosecond tunnelling interferometry *Nature Physics* **11** 815-819
[39] Shafir D., Soifer H., Bruner B. D., Dagan M., Mairesse Y., Patchkovskii S., Ivanov M. Yu., Smirnova O. and Dudovich N. 2012 Resolving the time when an electron exits a tunnelling barrier *Nature* **485** ((7398)) 343
[40] Cireasa R., Boguslavskiy A.E., Pons B., Wong M.C.H., Descamps D., Petit S., Ruf H., Thiré N., Ferré A., Suarez J., Higuet J., Schmidt B.E., Alharbi A., Légaré F., Blanchet V.,

Fabre B., Patchkovskii S., Smirnova O., Mairesse Y. and Bhardwaj V. R. 2015 Probing molecular chirality on a sub-femtosecond timescale *Nature Physics* **11** 654
[41] Ayuso D., Decleva P., Patchkovskii S. and Smirnova O. 2018 Chiral dichroism in bi-elliptical high-order harmonic generation *Journal of Physics B: Atomic, Molecular and Optical Physics* **51** 06LT01
[42] Ayuso D., Decleva P., Patchkovskii S. and Smirnova O. 2018 Strong-field control and enhancement of chiral response in bi-elliptical high-order harmonic generation: an analytical model *Journal of Physics B: Atomic, Molecular and Optical Physics* **51** 124002
[43] Smirnova O., Mairesse Y. and Patchkovskii S. 2015 Opportunities for chiral discrimination using high harmonic generation in tailored laser fields *Journal of Physics B: Atomic, Molecular and Optical Physics* **48** 234005
[44] Keldysh L V 1965 Ionization in the field of a strong electromagnetic wave *Sov. Phys.—JETP* 20 1307
[45] Perelomov A M, Popov V S and Terentév M V 1966 Ionization of atoms in an alternating electric field *Sov. Phys.—JETP* 23 924
[46] Perelomov A M, Popov V S and Terentév M V 1967 Ionization of atoms in an alternating electric field: II. *Sov. Phys.—JETP* 24 207
[47] Perelomov A M and Popov V S 1967 Ionization of atoms in an alternating electric field: III. *Sov. Phys.—JETP* 25 336
[48] Popruzhenko S. V. 2014 Keldysh theory of strong field ionization: history, applications, difficulties and perspectives *Journal of Physics B: Atomic, Molecular and Optical Physics* **47** 204001
[49] Ivanov M, Spanner M and Smirnova O 2005 Anatomy of strong field ionization *J. Mod. Opt.* **52** 165
[50] Keller J.B. 1958 *Calculus of Variations and its Applications Proceedings of Symposia in Applied Mathematics* vol 8 (New York: McGraw-Hill)
[51] Keller J B 1962 Geometrical theory of diffraction *J. Opt. Soc. Am.* **52** 116
[52] Norcliffe A, Percival I C and Roberts M J 1968 Correspondence identities: III. Classical paths and rutherford scattering *J. Phys. B: At. Mol. Phys.* **2** 578
[53] Pfeiffer A N, Cirelli C, Smolarski M, Wang X, Eberly J H, Dörner R and Keller U 2011 Breakdown of the independent electron approximation in sequential double ionization *New J. Phys.* **13** 093008
[54] Yuan J *et al* 2013 Tunnelling coordinates of high-energy photoelectrons in above-threshold ionization *J. Phys. B: At. Mol. Opt. Phys.* **47** 015003
[55] Li M *et al* 2016 Subcycle nonadiabatic strong-field tunneling ionization *Phys. Rev.* A **93** 013402
[56] Ivanov I A, Nam C H and Kim K T 2017 Exit point in the strong field ionization process *Sci. Rep.* **7** 39919
[57] Han M *et al* 2017 Tunneling wave packets of atoms from intense elliptically polarized fields in natural geometry *Phys. Rev.* A **95** 023406
[58] Perelomov A M, Kuzentsov V P and Popov V S 1968 Quasiclassical approximation for nonstationary problems *Sov. Phys.—JETP* **26** 222
[59] Ivanov M. Yu., Spanner M. and Smirnova O. 2005 Anatomy of strong field ionization *Journal of Modern Optics* **52** 165-184
[60] Czirják A., Kopold R., Becker W., Kleber M. and Schleich W. 2000 The Wigner function for tunneling in a uniform static electric field *Optics Communications* **179** 29-38
[61] Tennyson J 2010 Electron-molecule collision calculations using the r-matrix method *Phys. Rep.* **491** 29
[62] Torlina L and Smirnova O 2012 Time-dependent analytical r-matrix approach for strong-field dynamics *Phys. Rev.* A **86** 043408
[63] Torlina L, Ivanov M, Walters Z B and Smirnova O 2012 Time-dependent analytical r-matrix approach for strong-field dynamics: II. Many-electron systems *Phys. Rev.* A **86** 043409
[64] Kaushal J and Smirnova O 2013 Nonadiabatic coulomb effects in strong-field ionization in circularly polarized laser fields *Phys. Rev.* A **88** 013421
[65] Torlina L, Kaushal J and Smirnova O 2013 Time-resolving electron-core dynamics during strongfield ionization in circularly polarized fields *Phys. Rev.* A **88** 053403
[66] Torlina L, Morales F, Kaushal J, Ivanov I, Kheifets A, Zielinski A, Scrinzi A, Müller H G, Ivanov M and Smirnova O 2015 Interpreting attoclock measurements of tunnelling times *Nat. Phys.* **11** 503
[67] Kaushal J, Morales F and Smirnova O 2015 Opportunities for detecting ring currents using an attoclock setup *Phys. Rev.* A **92** 063405
[68] Torlina L and Smirnova O 2017 Coulomb time delays in high harmonic generation *New J. Phys.* **19** 023012
[69] Popruzhenko S. V. 2018 Coulomb phase in high harmonic generation *Journal of Physics B: Atomic, Molecular and Optical Physics* **51** 144006
[70] Kaushal J, Morales F, Torlina L, Ivanov M and Smirnova O 2015 Spin–orbit larmor clock for ionization times in one-photon and strong-field regimes *J. Phys. B: At. Mol. Opt. Phys.* **48** 234002
[71] Kaushal J and Smirnova O 2018 Looking inside the tunnelling barrier: I. Strong field ionisation from orbitals with high angular momentum in circularly polarized fields *J. Phys. B: At. Mol. Opt. Phys.*
[72] Barth I and Smirnova O 2011 Nonadiabatic tunneling in circularly polarized laser fields: physical picture and calculations *Phys. Rev.* A **84** 063415
[73] Eckart S *et al* 2018 Ultrafast preparation and detection of ring currents in atoms *Nat. Phys.* **14** 701-704
[74] Goreslavski S P, Paulus G G, Popruzhenko S V and Shvetsov-Shilovski N I 2004 Coulomb asymmetry in above-threshold ionization *Phys. Rev. Lett.* **93** 233002
[75] Popruzhenko S. V., Paulus G.G. and Bauer D. 2008 Coulomb-corrected quantum trajectories in strong-field ionization *Phys. Rev. A* **77** 053409
[76] Camus N, Yakaboylu E, Fechner L, Klaiber M, Laux M, Mi Y, Hatsagortsyan K Z, Pfeiffer T, Keitel C H and Moshammer R 2017 Experimental evidence for quantum tunneling time *Phys. Rev. Lett.* **119** 023201